Article

Effect of the Solvate Environment of Lithium Cations on the Resistance of the Polymer Electrolyte/Electrode Interface in a Solid-State Lithium Battery

Alexander V. Chernyak [1,2,*], Nikita A. Slesarenko [1], Anna A. Slesarenko [1], Guzaliya R. Baymuratova [1], Galiya Z. Tulibaeva [1], Alena V. Yudina [1], Vitaly I. Volkov [1,2], Alexander F. Shestakov [1,3] and Olga V. Yarmolenko [1]

[1] Federal Research Center of Problems of Chemical Physics and Medicinal Chemistry RAS, 142432 Chernogolovka, Russia
[2] Scientific Center in Chernogolovka RAS, 142432 Chernogolovka, Russia
[3] Faculty of Fundamental Physical and Chemical Engineering, M. V. Lomonosov Moscow State University, 119991 Moscow, Russia
* Correspondence: sasha_cherniak@mail.ru

Abstract: The effect of the composition of liquid electrolytes in the bulk and at the interface with the LiFePO$_4$ cathode on the operation of a solid-state lithium battery with a nanocomposite polymer gel electrolyte based on polyethylene glycol diacrylate and SiO$_2$ was studied. The self-diffusion coefficients on the 7Li, 1H, and 19F nuclei in electrolytes based on LiBF$_4$ and LiTFSI salts in solvents (gamma-butyrolactone, dioxolane, dimethoxyethane) were measured by nuclear magnetic resonance (NMR) with a magnetic field gradient. Four compositions of the complex electrolyte system were studied by high-resolution NMR. The experimentally obtained ^{1}H chemical shifts are compared with those theoretically calculated by quantum chemical modeling. This made it possible to suggest the solvate shell compositions that facilitate the rapid transfer of the Li$^+$ cation at the nanocomposite electrolyte/LiFePO$_4$ interface and ensure the stable operation of a solid-state lithium battery.

Keywords: polymer electrolyte; nanocomposite; organic electrolyte; solid-state lithium battery; solvate shell; NMR; self-diffusion coefficients; chemical shifts; quantum chemical modeling

1. Introduction

The preparation of solid-state batteries is one of the solutions to the safety problems of lithium and lithium-ion batteries (LIBs) [1–9]. However, in solid-state devices, each stage of charge transfer, from the diffusion of ions in the electrolyte and electrode materials to the charge transfer across the porous electrode-electrolyte interface, is significantly hindered. At the same time, the lithium metal/polymer electrolyte interface does not form a solid electrolyte interface (SEI) on the lithium surface due to the absence of a liquid organic phase [10–13].

To eliminate the problem of poor electrode/solid electrolyte contact, we used "Liquid phase therapy" [14–22]. "Liquid-phase therapy" consists of the introduction of liquid electrolytes to increase ion transport and stability at the interface. The process of ion transfer is carried out only in a solid-state electrolyte. This approach is used for systems where porous structures such as a carbon anode, LiFePO$_4$ or LiCoO$_2$ cathodes, and solid inorganic electrolytes or their hybrids with polymers act as electrode materials [23–27]. Here, poor contact between solid electrolytes and electrodes is caused by their different surface morphology.

The mechanism of "liquid-phase therapy" consists of several stages:

(1) first, the lithium ion must pass from a solid (polymer, ceramic, or composite) electrolyte into a solvate shell of solvent molecules;

(2) then the solvated lithium ions are adsorbed on the electrode surface;

(3) then their partial desolvation and migration over the cathode surface with the remaining solvent molecules occur;

(4) and, finally, the detachment of the last solvent molecules and the introduction of a lithium ion into the electrode lattice take place.

In total, taking into account "liquid-phase therapy", several interface boundaries can be observed in lithium solid-state batteries [28–33]: (1) solid electrolyte/lithium anode, (2) solid electrolyte/cathode, (3) liquid electrolyte/cathode, and (4) solid electrolyte/liquid electrolyte.

Solid-to-solid interfacial contact for the first boundary (with lithium) leads to a slow migration of ions. At the same time, for the polymer electrolyte/lithium contact, a minor number of dendrites are formed on the anode surface as was already mentioned above [10–13]. In the case of the lithium interface with nanocomposite polymeric gel electrolytes [34–40], the charge transfer resistance decreases for two reasons. First, the polymer electrolyte–lithium contact does not lead to the growth of SEI of a large thickness as occurs in the liquid phase. Second, oxide nanoparticles (SiO_2, TiO_2, Al_2O_3, etc.) are able to form nanostructures at the interface with lithium and to form favorable pathways for the transport of lithium ions. Therefore, in the case of using NPE, "liquid-phase therapy" at the border with lithium is superfluous.

At the solid electrolyte/cathode interface [41], it is already necessary to use "liquid-phase therapy" because of lacking tight contact. In the future, a new interface boundary the liquid electrolyte/cathode appears. Here, the transfer resistance of Li^+ ions mainly depends on the cathode. The structure of the cathode during the charge-discharge process also greatly affects the intercalation and extraction of Li^+ ions.

Thus, the preparation of a solid-state lithium battery with a nanocomposite gel electrolyte looks very promising. Polymer nanocomposite electrolytes (NPEs) [42–44] are among the promising classes of polymer electrolytes. They combine the advantages of gel electrolytes (high conductivity in the liquid phase) and composite electrolytes (good mechanical properties and a wide window of electrochemical stability).

In [45–48], we developed and studied a number of new NPEs based on a three-dimensional network matrix with ethylene oxide units, a large amount of liquid electrolyte (about 80 wt.%), and SiO_2 nanoparticles (Aerosil 380). These nanoparticles, as shown in [48–50], have the property of increasing the number of charge carriers due to ionic dissociation on their developed surface.

NPE based on 15 wt.% polyethylene glycol diacrylate, 1 M $LiBF_4$ in gamma-butyrolactone with 2–10 wt.% SiO_2 nanoparticles had attractive properties, namely, high conductivity of 1–3 mS cm^{-1} at temperatures from −70 to +100 °C, high self-diffusion coefficients on ^{7}Li (1.2×10^{-10} m^2 s^{-1}), and transfer numbers for the lithium cation up to 0.49 [45–48].

In [51], the composition of this NPE for operation in a Li/$LiFePO_4$ solid-state battery was optimized. A way to reduce the resistance at the NPE/$LiFePO_4$ interface was found experimentally. A high discharge capacity of ~170 mAh g^{-1} at C/10 (18 mA g^{-1}) by modifying the $LiFePO_4$ cathode surface with a liquid electrolyte of the 1 M LiTFSI in dioxolane/dimethoxyethane (1:1 *v/v*) was achieved. However, the nature of this effect remains unclear. It was more logical to assume that the composition of the liquid electrolyte for wetting the interface with $LiFePO_4$ should be similar to that included in the NPE. Here it turned out, on the contrary, that when wetting with an electrolyte of a similar composition, the interface "does not work", and when wetting with a completely different electrolyte (both salt and solvent change), the interface "opens". A change in the composition of the electrolyte leads to a change in the solvate environment of Li^+ ions, which takes part in electrode reactions [52–54].

In order to reveal possible reasons for the observed effect, in this work the influence of the solvate environment of lithium cations on the resistance of the NPE/$LiFePO_4$–cathode interface was studied. In addition, high-resolution NMR and pulsed magnetic field gradient (PGM) NMR techniques in combination with quantum chemical modeling of solvate complexes in various solvents were applied.

The NMR method [55,56] and theoretical research methods (quantum chemistry, molecular dynamics) [57–60] were used to understand the state of Li$^+$ ions in solution, since they are very informative for studying the mechanisms of processes occurring in LIBs.

2. Materials and Methods

2.1. Materials

LiBF$_4$ (purity 98%); lithium bis(trifluoromethanesulfonyl)imide, and LiTFSI (purity 99%, water $\leq$ 1%) were used as electrolyte salts; gamma-Butyrolactone, (GBL, purity > 99%, water < 0.005%), 1,3-dioxolane (DOL, purity 99.8%) and dimethoxyethane (DME, purity 99%, water < 0.005%) were used as electrolyte solvents. All chemical reagents and diluents were acquired from Sigma-Aldrich (St. Louis, MO, USA) and used as received. N-Methylpyrrolidone (NMP, Fluka) was used to prepare the cathode mass. Polyethylene glycol diacrylate (PEG-DA, Aldrich, M$_n$ = 575, T_g = −73.5 °C) was used to obtain a three-dimensional network matrix for the polymer electrolyte. The radical polymerization initiator, benzoyl peroxide (PB, Aldrich), stored in water (30%) was recrystallized from chloroform followed by drying at 20 °C in air and then in a vacuum. SiO$_2$ nanoparticles (Aerosil 380, surface area 380 m^2 g^{-1}, average particle size 7 nm) were used to fill the electrolyte polymer matrix. Lithium foil (JSC "Lithium-element", Saratov, Russia) 1 mm thick was the anode material. The cathode components were as follows:(1) LiFePO$_4$ (MTI Corporation, Richmond, CA, USA), purity >97%, particle size less than 5 μm, (2) conductive carbon black Timical Super C65 (MTI Corporation, USA, S$_{sp}$ = 80 m^2 g^{-1}, particle size 60 μm, and (3) polyvinylidene difluoride (PVDF) polymer binder (Kynarflex HSV 900, Arkema, Colombes, France, MM > 100,000, density 1.76 g cm^{-3}).

2.2. Liquid Electrolytes

The compositions of the electrolytes prepared for the study are given in Table 1.

**Table 1.** Compositions of liquid electrolytes.

No.	Electrolyte	Abbreviation
1	1 M LiBF$_4$ in GBL	LiBF$_4$—GBL
2	1 M LiBF$_4$ in DOL/DME (1:1 *v/v*)	LiBF$_4$—DOL/DME
3	1 M LiTFSI in DOL/DME (1:1 *v/v*)	LiTFSI—DOL/DME
4	1 M LiBF$_4$ in GBL + 1M LiTFSI in DOL/DME (1:1 *v/v*)	LiBF$_4$—LiTFSI—GBL/DOL/DME

The conductivity of an organic electrolyte was measured by conductometry on an LCR819 immittance meter (Goodwill Instruments Ltd., Taiwan) at an alternating current of 1 kHz in a glass electrochemical cell with plate-like platinum electrodes.

2.3. Synthesis of Nanocomposite Polymer Electrolyte

The nanocomposite polymer electrolyte was synthesized by the radical polymerization of PEG-DA in the presence of the radical initiator PB.

PEG-DA
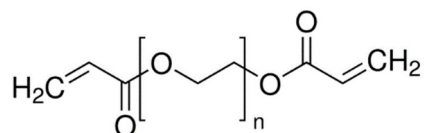
The composition of the polymerizable mixture (wt.%) was as follows: 15 PEG-DA, 78 [1 M LiBF$_4$ in GBL], 6 SiO$_2$, 1 PB. The curing of this mixture was carried out on the basis of studying the kinetics of polymerization [45] according to the following regime: 60 °C; for 3 h, 70 °C for 1 h, 80 °C for 1 h, and 120 °C for 1 h [51].

2.4. Electrode Preparation and Cell Assembly

Lithium as an anode in the form of a disk 16 mm in diameter and 1 mm thick was used. The cathodes were prepared from three components, namely, $LiFePO_4$: carbon black: PVDF = 75:20:5 wt.%. PVDF was dissolved in NMP at the ratio of 2.5 mL of the solvent per 1 g of the cathode material with magnetic stirring at 50 °C. Then a weighed amount of conductive carbon black and $LiFePO_4$ was added. The prepared mixture was applied onto graphitized Al foil using the Doctor Blade method (Dongguan city, China, Gelon) and then it was dried at 150 °C for 4 h. Next, the cathodes were pressed on rollers, and then it was dried for 8 h at a temperature of 120 °C in a vacuum oven.

Coin—CR2032 cells were assembled in an MBraun argon box (Germany). Symmetrical $LiFePO_4//LiFePO_4$ cells for studies by the electrochemical impedance method were used. Full $Li//LiFePO_4$ cells for studies by the galvanostatic cycling method were used. An NPE membrane of the same diameter was placed between the cathode and anode.

2.5. Cell Testing

Electrochemical impedance measurements in symmetrical $LiFePO_4//LiFePO_4$ cells using a Z-2000 Elins impedance meter (Russia) (frequency interval 1 Hz to 600 kHz) with a signal amplitude of 10 mV were performed. Impedances are measured one week after assembling at ambient temperature.

The $Li//LiFePO_4$ cells were tested on a BTS 5V10mA device (Shenzhen Neware electronic Co., Ltd., Shenzhen, China) in the galvanostatic mode at a current rate of C/10 in a range of 2.6–3.8 V.

2.6. NMR with Pulsed Magnetic Field Gradient

The NMR measurements on a Bruker Avance-III 400 MHz NMR spectrometer equipped with the diff60 gradient unit (the maximum field gradient amplitude was 30 T/m) were carried out at the temperature 22 ± 1 °C. The NMR measurements of ^1H (diffusion of solvent molecules), ^7Li (diffusion of lithium cations), and ^{19}F (diffusion of anions) were carried out with operating frequencies of 400, 155.5, and 376.5 MHz, respectively. The stimulated spin-echo sequence was applied. The details of self-diffusion coefficient measurements are given in [61,62]. The experimental NMR parameters of pulse sequences were the following: $\pi/2$ pulse was 9.5 μs (^1H), 9 μs (^7Li), and 10 μs (^{19}F); gradient pulse duration time δ was 1–1.5 ms; and the diffusion 32 steps with maximum field gradient amplitude g were 3.5 (^1H), 11.5 (^7Li), and 4.0 (^{19}F) T/m. The measurement error of the self-diffusion coefficients was 5%.

2.7. High-Resolution NMR

High-resolution spectra for ^1H, ^7Li, ^{11}B, ^{13}C, and ^{19}F were recorded on a Bruker Avance III 500 MHz NMR spectrometer. The measurements at frequencies of 500, 194, 160, 126, and 471 MHz for ^1H, ^7Li, ^{11}B, ^{13}C, ^{17}O, and ^{19}F, respectively, were carried out at room temperature (22 ± 1 °C). Liquid samples in standard 5 mm NMR tubes without adding a deuterium solvent were placed. The chemical shift scale was calibrated with the DMSO-d_6 signal in the capillary as an external standard (2.50 ppm for ^1H). The ^1H, ^7Li, ^{11}B, and $^{19}FNMR$ spectra were obtained using the standard sequence $\pi/2$ pulses, FID. No signal accumulation was applied. To obtain the $^{13}CNMR$ spectra, a standard sequence from the TopSpin (Bruker) zgpg30 library was used. The sequence is an accumulation of signals from 300 pulses with the suppression of the ^1H spin-spin interaction for the duration of all the experimental times. The number of repetitions was ns = 512, and the delay between the repetition sequence was d1 = 1.5 s.

2.8. Quantum Chemical Modeling

The structure of solvate complexes of lithium cations with solvent molecules was studied using the nonempirical Perdew–Burke–Erzernhof (PBE) exchange-correlation functional [63] using the extended basis H [5s1p/2s1p], C, N, O, F, S [5s5p2d/3s3p2d], Li [4s1p/2s1p] for valence electrons and SBK pseudopotential [64]. The geometry of larger

systems containing a counterion and additional solvent molecules was optimized using the effective Hamiltonian method [65] taking into account the van der Waals interaction. Chemical shifts for optimized structures were calculated using the $\Lambda 2$ basis set of cc-pVTZ quality [66]. The Priroda package [67] was used for all the calculations carried out at the Joint Supercomputer Center of the Russian Academy of Sciences.

3. Results and Discussion

3.1. Investigation of the NPE/LiFePO$_4$-Cathode Interface

At the first stage, the NPE/LiFePO$_4$ interface was studied by the method of electrochemical impedance in symmetrical LiFePO$_4$//LiFePO$_4$ cells. The coin-type cells were assembled with an NPE membrane and various LiFePO$_4$ cathode surface treatments. The cell compositions are shown in Table S1, ESI. The Nyquist plots of the studied cells are shown in Figure 1.
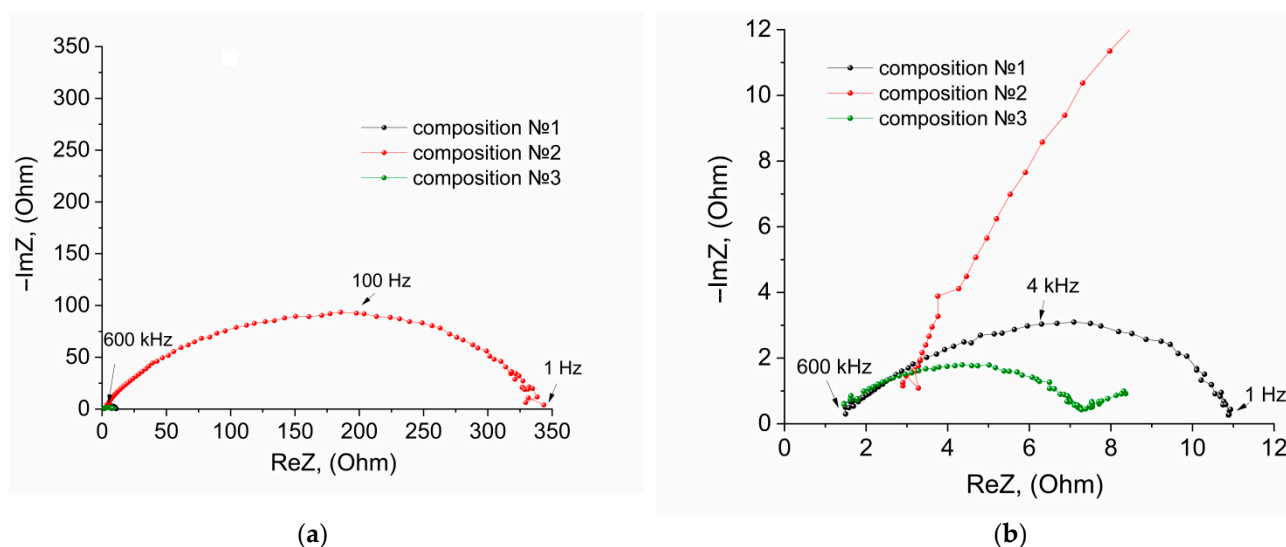

Figure 1. Nyquist plots of the impedance of the LiFePO$_4$//LiFePO$_4$ cells, where (**a**) general view and (**b**) view on an enlarged scale. Composition: (1) LiFePO$_4$/NPE/LiFePO$_4$; (2) LiFePO$_4$/NPE/LiBF$_4$—GBL/LiFePO$_4$; (3) LiFePO$_4$/NPE/LiTFSI—DOL-DME/LiFePO$_4$.

The equivalent circuits for the Nyquist plots of 1–3 cells (Figure 1) were selected (Table S1, ESI). Table S2, ESI presents the results of calculating the parameters of equivalent circuits using the ZView2 software.

The electrolyte LiBF$_4$–GBL for the preparation of NPE was chosen., The LiBF$_4$ salt is thermally stable and suitable for the synthesis of polymer electrolytes by radical polymerization in contrast to the LiPF$_6$ salt, which is prone to decomposition with the formation of PF$_5$ [68]. This Lewis acid is the initiator of a parallel process of ionic polymerization, which ultimately leads to the deterioration of the conductive properties of polymer electrolytes [69].

The equivalent circuits of the Nyquist plots of the cells with NPE and NPE/LiTFSI-DOL-DME contain a closed Warburg element (Tables S1 and S2, ESI). That is, at low frequencies, a large number of ions that have reached the opposite electrode can intercalate into LiFePO$_4$.

Figure 1 and Table S2, ESI show the resistance at the electrolyte/LiFePO$_4$ interface, which is minimum for composition No. 3. Therefore, the NPE and surface treatment of LiFePO$_4$ cathodes with the LiTFSI-DOL-DME electrolyte were chosen for testing in battery prototypes.

3.2. Li/NPE/LiFePO₄ Cells Cycle Tests

Based on the electrochemical impedance data, two types of Li/NPE/LiFePO$_4$ cells were assembled and are shown in Figure 2, where LE is the liquid electrolyte.
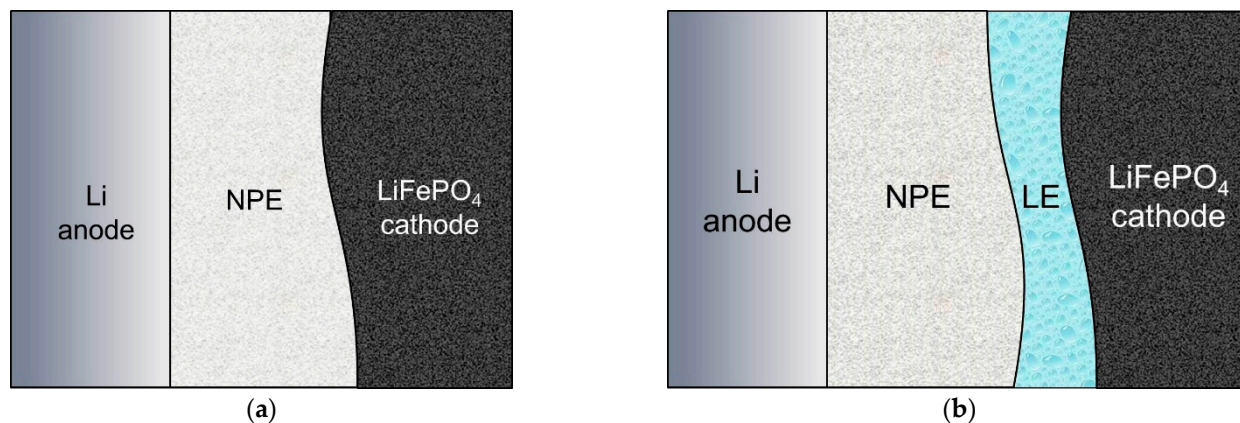

(**a**)　　　　　　　　　　　　　　　　　　　　　　　　　(**b**)

Figure 2. Assembly diagram of the Li/NPE/LiFePO$_4$ cells, where (**a**) LiFePO$_4$ surface was not treated in any way ("dry assembly"); (**b**) the surface of the LiFePO$_4$ cathode was treated with a LiTFSI solution in DOL-DME.

Figure 3 shows the charge-discharge profiles of Li//LiFePO$_4$ cells of both types. Cycling was carried out in the voltage range of 2.6–3.8 V since a 1 M solution of LiTFSI in DOL/DME (1:1) has an electrochemical stability up to 3.8 V vs. Li$^+$/Li [70].

(**a**)　　　　　　　　　　　　　　　　　　　　　　　　　(**b**)
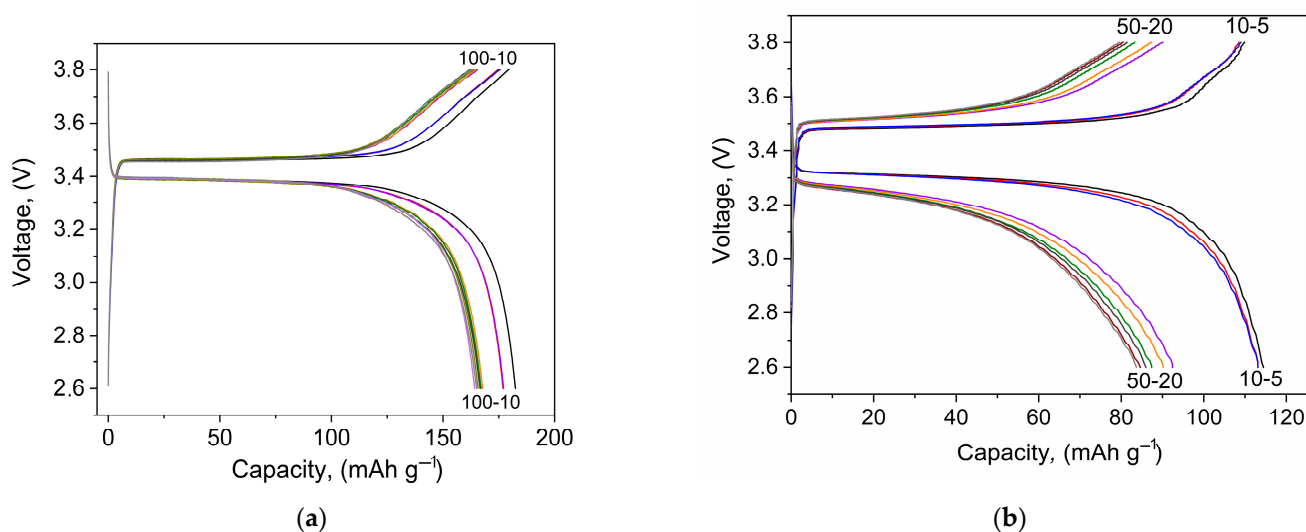
Figure 3. Charge and discharge curves of the Li//LiFePO$_4$cells, where (**a**) with LiTFSI–DOL-DME and (**b**) "dry assembly" at the C/10 current rate in a voltage range of 2.6–3.8 V.

Figure 3 shows that, when treated with a liquid electrolyte, the distance between the charge and discharge plateaus decreases to 0.09 V compared to the "dry assembly", where this value is 0.25 V. The larger voltage separation is due to a higher resistance at the electrode/electrolyte interface.

Figure 4 shows the dependence of the discharge capacity on the cycle number of the Li/NPE/LiFePO$_4$ cells for different assemblies (Figure 2).

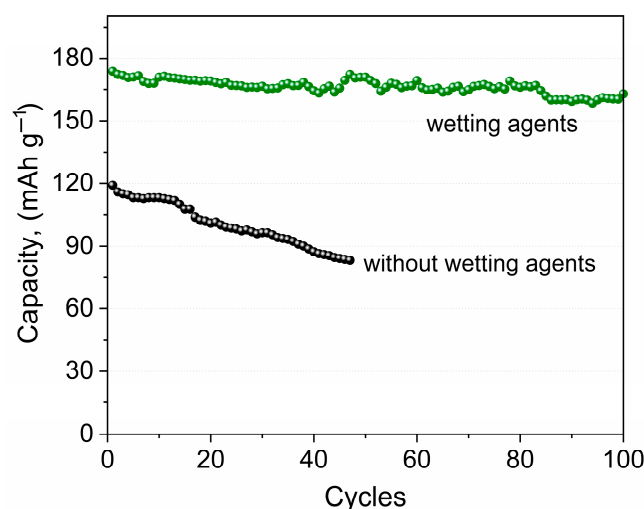**Figure 4.** Dependence of the discharge capacity on the cycle number for the Li//LiFePO$_4$ cells, NPE with liquid electrolyte 1 M LiTFSI DOL/DME (1:1) (green line) and without it (black line) at the C/10 current rate in a voltage range of 2.6–3.8 V.

3.3. The Self-Diffusion Coefficients. Pulse Field Gradient of NMR (PFG NMR)

The self-diffusion coefficients D$_s$ were measured by PFG NMR using the stimulated spin echo pulse train method. The dependences of the spin echo damping $A(2\tau_1, \tau_2, g)$ on the squared amplitude of the magnetic field gradient g^2 (diffusion decay) were analyzed. The diffusion decay was exponential. The diffusion decays were approximated by the exponent.

$$A(2\tau_1, \tau_2, g) = \exp\left(-\gamma^2 \cdot g^2 \cdot \delta^2 \cdot t_d \cdot D_s\right) \tag{1}$$

where D_s is the self-diffusion coefficient, $A(2\tau_1, \tau_2, g)$ is the intensity of the "spin echo" signal, g is the magnetic field gradient amplitude, γ is the gyromagnetic ratio of the nucleus under study, δ is the gradient pulse duration, and t_d is the diffusion time.

Figure 5 shows the diffusion decay on ^{1}H, ^{19}F, and ^{7}Li nuclei. Table 2 presents the results of measuring the diffusion coefficients.

Table 2. Self-diffusion coefficients on ^{7}Li, ^{19}F, and ^{1}H (m^2 s^{-1}) and experimental conductivity at room temperature.

Sample	LiBF$_4$ (^{7}Li)	LiTFSI (^{7}Li)	LiBF$_4$ (^{19}F)	LiTFSI (^{19}F)	GBL (^{1}H)	DOL (^{1}H)	DME (^{1}H)	Conductivity, mS cm^{-1}
(1) LiBF$_4$—GBL	1.8×10^{-10}		2.5×10^{-10}		4.0×10^{-10}			8.0
(2) LiBF$_4$—DOL/DME	6.8×10^{-10}		7.0×10^{-10}			1.6×10^{-9}	1.3×10^{-9}	5.7
(3) LiTFSI—DOL/DME		4.7×10^{-10}		4.0×10^{-10}		1.1×10^{-9}	7.3×10^{-10}	9.4
(4) LiBF$_4$—LiTFSI—GBL/DOL/DME		3.3×10^{-10}	3.6×10^{-10}	3.9×10^{-10}	6.4×10^{-10}	8.5×10^{-10}	6.5×10^{-10}	10
(5) Solvents					7.2×10^{-10}	2.1×10^{-9}	2.8×10^{-9}	
(6) DOL/DME(1:1)						2.0×10^{-9}	2.2×10^{-9}	
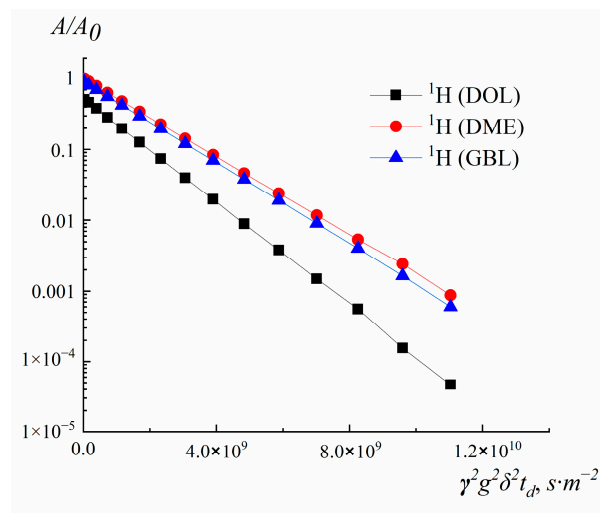
(**a**)
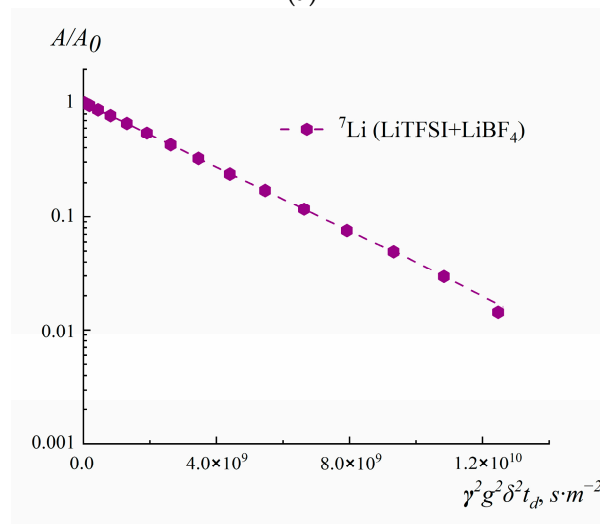
(**b**)
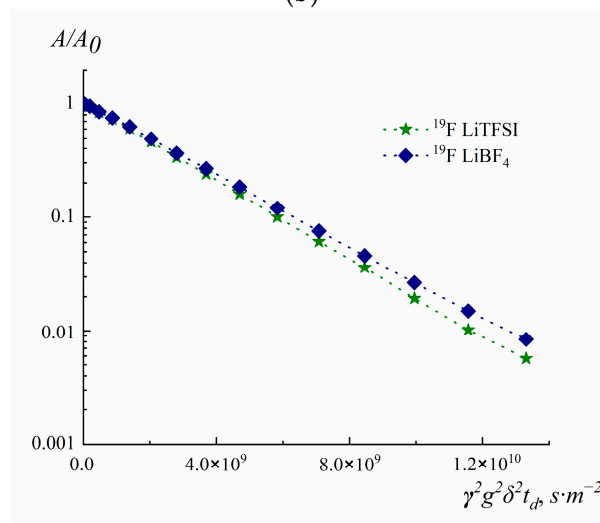
(**c**)

Figure 5. Diffusion decays on (**a**) ^{1}H, (**b**) ^{7}Li and (**c**) ^{19}F.

Diffusion attenuations on ^{1}H were recorded from the fading of signals of the solvent. Depending on the composition of the electrolyte, signals from different solvents were used: GBL, DOL, and DME (Figure 5a). Thus, the ^{1}H diffusion coefficients (D_s) correspond to the mobility of the solvent molecules GBL, DOL, and DME, depending on the signal selected for diffusion decay.

Only one signal is observed in the ^{7}Li NMR spectra in the salts mixture (Figure 5b). Therefore, it is impossible to obtain the diffusion coefficients D_s of Li$^+$ cations for LiBF$_4$ and LiTFSI separately. For the composition LiBF$_4$-LiTFSI-GBL/DOL/DME, the measured diffusion coefficient on ^{7}Li corresponds to the average value of the mobility of Li$^+$ in LiBF$_4$ and LiTFSI (Figure 5b).

An analysis of diffusion experiments on ^{19}F (Figure 5c) allowed us to determine the average diffusion coefficient of the solvated anion BF$_4{}^-$ and the ion pair Li$^+$BF$_4{}^-$ (diffusion attenuation of the ^{19}F signal is -155 ppm). The average diffusion coefficient of the solvated anion TFSI$^-$ and the ion pair Li$^+$TFSI$^-$ (diffusion signal attenuation ^{19}F is -80 ppm) was also determined from the graph (Figure 5c).

As can be seen from the data obtained, the Li$^+$ cations and BF$_4{}^-$ anions in the GBL solvent have the lowest diffusion mobility. This is probably due to the highest solvation ability of GBL among all solvents used. GBL molecules have the lowest mobility: $D_s = 4.0 \times 10^{-10}$ m^2 s^{-1} (composition 1) vs. D_s for DOL and DME molecules, 1.4×10^{-9} m^2 s^{-1} and 1.0×10^{-9} m^2 s^{-1} correspondingly, in average for compositions 2 and 3. However, in the case of a mixture of all three types of solvents (composition 4), their mobility becomes more comparable $4 \times 10^{-10}-9 \times 10^{-10}$ m^2 s^{-1}. There is the highest decrease in DME self-diffusion coefficients in comparison with their values for DOL and GBL when changing from pure solvents to electrolyte solutions. Probably this is because of their ability to form chelate complexes (See Figure 6).

In the case of LiTFSI, the mobility of the cation and anion changes are comparable for compositions 3 and 4. At the same time, for LiBF$_4$, the change to DOL/DME solution (composition 2) leads to a significant increase (by a factor of 3–4) in both cationic and anionic mobility with respect to composition 1. This is not only the effect of significantly higher mobility of DOL and DME molecules, which is higher than the mobility of GBL molecules but is associated with the formation of more mobile ion pairs as well.

The self-diffusion coefficients of solvents were determined individually (row 5 of Table 2) and in the DOL/DME mixture (row 6 of Table 2). DOL and DME molecules have the highest diffusion coefficients, and their mobility slightly decreases when a mixed solution of DOL/DME (1:1) is formed.

In the electrolytes the mobility of DOL and DME molecules of solvents is reduced two or more times due to their involvement in the coordination sphere of less mobile ions and the effect is less pronounced for LiBF$_4$ solution (composition 2). In this case, the conductivity is the lowest due to the excess formation of neutral ion pairs of Li$^+$BF$_4{}^-$. Apparently, they have less strongly bound solvate shells, in contrast to ions. Accordingly, the proportion of free solvent molecules increases, which is accompanied by an increase in their diffusion coefficients (for DOL by 1.45 times, for DME by 1.78 times) in comparison with LiTFSI solution in DOL/DME with the highest conductivity. This is comparable to the increase in the mobility of ^{7}Li by a factor of 1.45 and that of ^{19}F by a factor of 1.75.

The self-diffusion coefficients of DOL and DME in composition 2 are approximately equal to the average of their values in composition 3 and a pure DOL/DME mixture. This is consistent with the assumption about the formation of ion pairs and the release of pure solvent in the case of composition 2.

There is some enhancement of GBL molecule mobility in composition 4 in comparison with pure GBL solvent; this may be associated with more strong pair interactions of GBL molecules with high dipole moments. In this GBL/DOL/DME mixed solvent, one should expect a decrease in the proportion of GBL associates due to entropy effects in dilute GBL solution and a corresponding increase in the content of more mobile non-associated GBL molecules.

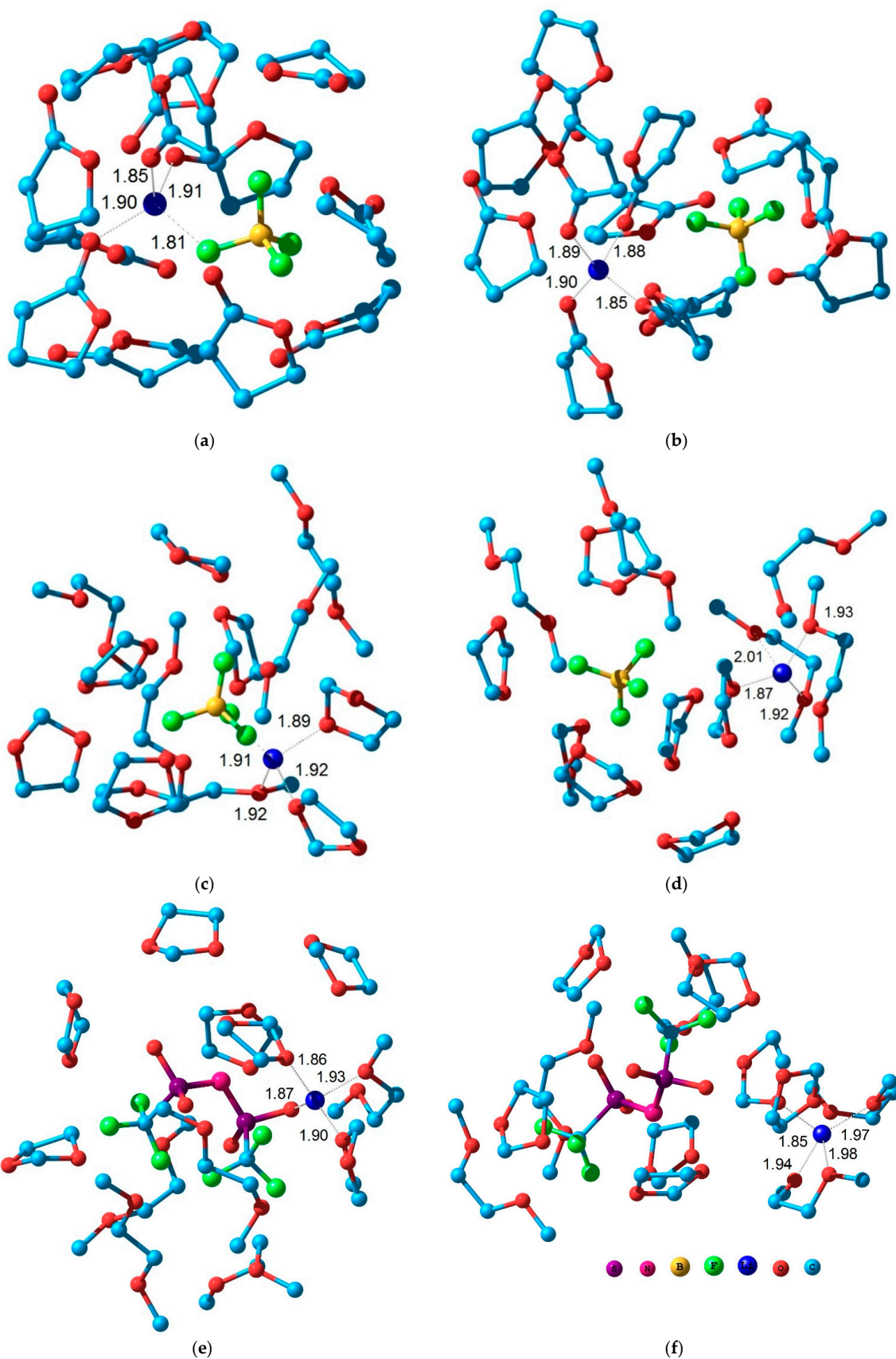**Figure 6.** Structure of the model solvate complex including the ion pair (**a**,**c**,**e**) and separated ions (**b**,**d**,**f**) for the electrolytes: LiBF$_4$ in GBL (**a**,**b**); LiBF$_4$ in DOL/DME (**c**,**d**) and LiTFSI in DOL/DME (**e**,**f**).

3.4. High-Resolution NMR

Tables 3 and 4 show the ^{1}H and ^{13}C chemical shifts for the solvents, respectively. Figures S1–S4, ESI show the ^{1}H and ^{13}C spectra of pure solvents and their mixtures along with their assignment to specific atoms of the structures.

Table 3. Experimental ^{1}H chemical shifts of the solvent and electrolyte samples (in ppm).

Solvents				Electrolytes			
GBL	DOL	DME	DOL + DME	No. 1	No. 2	No. 3	No. 4
4.09				4.08			4.14
2.23				2.22			2.27
2.01				1.98			2.03
	4.58		4.72		4.67	4.66	4.59
	3.57		3.71		3.68	3.67	3.61
		3.61	3.38		3.38	3.40	3.31
		3.45	3.22		3.21	3.22	3.12

Table 4. Experimental ^{13}C chemical shifts of the solvent and electrolyte samples (in ppm).

Solvents				Electrolytes			
GBL	DOL	DME	DOL + DME	No. 1	No. 2	No. 3	No. 4
177.70				179.00			179.03
68.19				68.69			68.83
26.91				27.05			27.27
21.54				21.37			21.62
	94.08		94.22		94.08	94.08	94.30
	63.66		63.80		63.77	63.75	64.03
		71.67	71.35		70.80	70.72	70.97
		57.84	57.55		57.61	57.71	57.87

Table 5 shows the [7]Li, [11]B, and ^{19}F chemical shifts of the electrolyte samples.

Table 5. Experimental chemical shifts of the electrolyte samples (in ppm).

Electrolytes	[7]Li	[11]B	[19]F	
No. 1	−0.45	−1.47	−154.94	−154.99
No. 2	−1.45	−1.37	−155.54	−155.60
No. 3	−1.69	-	−80.19	
No. 4	−0.87	−1.43	−80.06 −155.18	−155.24

Figures S5–S9, ESI show the ^{1}H, ^{7}Li, ^{11}B, ^{19}F, and ^{13}C NMR spectra along with their assignment to specific atoms of the structures.

3.5. Results of Quantum Chemical Modeling

The simplest molecular models containing one cation, one anion, and 12 solvent molecules (12 GBL molecules or 7 DOL molecules and 5 DME molecules) were used to study the structure of solvate complexes in various solvents. This stoichiometry corresponds to the composition of a 1 M solution. The van der Waals interaction of molecules in a liquid plays an important role and, therefore, it should be taken into account for a correct description of solvate complexes. For this purpose, the effective Hamiltonian method [65] was used. This technique takes into account the contribution of van der Waals interactions and is not inferior in accuracy to more time-consuming calculations by the density functional method [71]. Two types of structures containing a contact ion pair and a cation and anion separated by solvent molecules were considered. Figure 6 shows the structures of these model solvate complexes.

For the structures obtained, the magnetic shielding constants of the nuclei were calculated. Since solvate complexes differing in the arrangement and orientation of solvent

molecules have similar energies, the shielding constants were averaged over several structures. This approach gives a reasonable description of ^{1}H chemical shifts for pure solvents, which are modeled by clusters of 12 molecules: GBL: 2.44, 2.58, and 4.83 ppm; DOL/DME: 3.87, 5.21 ppm/3.36, 3.57 ppm. The theoretical values of chemical shifts have an inevitable error. To reduce it, when comparing the results for two types of solvate complexes, the following technique was applied.

In order to reproduce exactly the average value for all chemical shifts of nuclei of a certain type of the selected solvent molecule (*C*) and in the maximal spread (the difference between the maximum and minimum chemical shift values) (*S*) the following correction function was chosen for pure solvents:

$$\widetilde{\delta}_i = C_{exp} + \frac{S_{exp}}{S_{theor}}(\delta_i - C_{theor}) \tag{2}$$

where $\widetilde{\delta}_i$ is the corrected chemical shift for the *i*-th nucleus, and δ_i is the calculated chemical shift. The corrected values of ^{1}H chemical shifts for different types of solvent molecules were calculated (see Table S3, ESI) using this equation.

As a result, for a solution of LiBF$_4$ in GBL, the theoretical ^{1}H chemical shifts for separated ion pairs are in better agreement with the experimental ones than for contact ion pairs: the root-mean-square error is 0.17 and 0.21 ppm, respectively.

For other cases, the situation is reversed: the data for contact ion pairs somewhat better describe the experimental data for solutions of LiBF$_4$ and LiTFSI in DOL/DME; the corresponding root-mean-square differences are 0.16, 0.24 and 0.18, 0.19 ppm, respectively. Thus, the results of quantum chemical modeling are consistent with the NMR data on the mobility of various ions from which a higher degree of dissociation of LiBF$_4$ in GBL follows. A small increase in conductivity for a LiTFSI solution in DOL/DME compared to a LiBF$_4$ solution in GBL can be associated with a significant increase in the mobility of ions, which is compensated by their smaller number.

During the electrode reaction, the Li$^+$ ion is transferred from the solvate complex to the electrode surface at the anode. As the final state of the process is the same for different electrolytes, the corresponding energy change is determined mainly by the formation energy of the Li$^+$ solvation complex. Apparently, the transfer process is activated by the formation of a coordination vacancy in the solvate complexes. This allows one to form the first intermediate structures of Li$^+$ ion transfer, which are responsible for the Li$^+$ transfer to the layer surface that becomes possible in this case.

These energies of various Li$^+$ solvate complexes with GBL and DOL/DME molecules were found using the PBE density functional method (see Table S4, Figure S10, ESI). The main conclusions are the following. First, the solvate complexes in GBL are more stable compared to the solvate complexes of DOL/DME. Second, higher energy is required for the formation of a vacancy in the coordination sphere by the removal of one of the solvent molecules: 14 and 3–9 kcal/mol, respectively. From these data, the effect of "liquid-phase therapy" can be related to a lower reaction overvoltage at the cathode due to the higher energetic availability of lithium ions in the DOL/DME solvent.

4. Conclusions

The resistance of the interface between an electrode based on LiFePO$_4$ and a nanocomposite polymer gel electrolyte (NPE) obtained by the polymerization of diacrylate polyethylene glycol in a 1 M solution of LiBF$_4$ in gamma-butyrolactone (GBL) with the addition of nanodispersed SiO$_2$ was measured by a.c. electrochemical impedance spectroscopy. It was found that the NPE/cathode interface has a high resistance, while the use of "liquid-phase therapy" by 1 M LiTFSI in a mixture of dioxolane/dimethoxyethane (DOL/DME) significantly reduces this resistance. The cycling efficiency of the Li/NPE/LiFePO$_4$ cells was studied. It was found that in the presence of 1 M LiTFSI in DOL/DME at the interface with the cathode, both the discharge capacity and the cycle performance significantly increase.

The self-diffusion coefficients of solvent molecules, as well as the Li+ cation and anions in solutions of 1M $LiBF_4$ in GBL and DOL/DME, 1M LiTFSI in DOL/DME, and also in a mixture of 1M $LiBF_4$ in GBL + 1M LiTFSI in DOL/DME, which models the composition at the NPE/liquid electrolyte interface, were measured. From the data obtained, it follows that a higher rate of salt dissociation is found in GBL, and higher ion mobility is found in a DOL/DME mixture.

It follows from the performed quantum chemical calculations that the effect of "liquid-phase therapy" at the NPE/1M LiTFSI interface in DOL/DME is due to the formation of more labile Li^+ solvate complexes in DOL/DME, which facilitates the transfer of Li+ from NPE through a liquid solution to the solid layer of the $LiFePO_4$ electrode.

Supplementary Materials: The following supporting information can be downloaded at: https://www.mdpi.com/article/10.3390/membranes12111111/s1, Table S1: Electrolyte Compositions and Equivalent Cell Circuits $LiFePO_4$//$LiFePO_4$; Table S2: Calculated parameters of equivalent circuits of cells 1–3; Figure S1: ^{1}H NMR (a) and ^{13}C NMR (b) high resolution spectrum of GBL; Figure S2: 1H NMR (a) and 13C NMR (b) high resolution spectrum of DOL; Figure S3: ^{1}H NMR (a) and ^{13}C NMR (b) high resolution spectrum of DME; Figure S4: ^{1}H NMR (a) and ^{13}C NMR (b) high resolution spectrum of DOL + DME; Assignment of NMR lines of solvent spectra; Figure S5: ^{1}H NMR spectrum of electrolytes (a) No. 1 (b), No. 2, (c) No. 3, (d) No. 4; Figure S6: ^{7}Li NMR spectrum of electrolytes (a) No. 1 (b), No. 2, (c) No. 3, (d) No. 4; Figure S7: ^{11}B NMR spectrum of electrolytes (a) No. 1 (b), No. 2, (c) No. 4; Figure S8: ^{13}C NMR spectrum of electrolytes (a) No. 1 (b), No. 2, (c) No. 3, (d) No. 4; Figure S9: ^{19}F NMR spectrum of electrolytes (a) No. 1 (b), No. 2, (c) No. 3, (d) No. 4; Assignment of NMR lines of electrolyte spectra; Table S3: Calculated and corrected values of ^{1}H chemical shifts of solvent molecules for different model solvate complexes in ppm; Table S4: Energies of formation at T = 0 K, d*E*, and enthalpies of formation d*H* at T = 298 K of solvate complexes; Figure S10: Calculated structure of solvate complex $Li(DME)_4^+$ (a), $Li(DME)_3^+$ (b), $Li^+(DOL)(DME)_3$ (c), $Li(DOL)_2(DME)_2$ (d), $Li(DOL)_3(DME)$ (e), $Li(DOL)_4$ (f), Li $(GBL)_4$ (d); Table S5: Cartesian coordination of calculated structures in Å.

Author Contributions: Conceptualization, O.V.Y.; methodology, A.V.C.; validation, N.A.S. and G.R.B.; formal analysis, G.Z.T. and A.F.S.; investigation, N.A.S. and A.A.S.; data curation, A.V.Y.; writing–original draft preparation, A.V.C. and O.V.Y.; writing–review and editing, A.V.Y. and O.V.Y.; visualization, N.A.S., A.A.S. and G.Z.T.; supervision, V.I.V.; Project administration, Funding A.V.C. and O.V.Y.; Acquisition, V.I.V. and A.F.S.; All authors have read and agreed to the published version of the manuscript.

Institutional Review Board Statement: Not applicable.

Data Availability Statement: Not applicable.

Conflicts of Interest: The authors declare no conflict of interest.

References

1. Lu, Y.; Zhao, C.-Z.; Yuan, H.; Hu, J.-K.; Huang, J.-Q.; Zhang, Q. Dry Electrode Technology, the Rising Star in Solid-State Battery Industrialization. *Matter* **2022**, *5*, 876–898. [CrossRef]
2. Lee, D.; Lee, H.; Song, T.; Paik, U. Toward High Rate Performance Solid-State Batteries. *Adv. Energy Mater.* **2022**, *12*, 2200948. [CrossRef]
3. Li, L.; Duan, H.; Li, J.; Zhang, L.; Deng, Y.; Chen, G. Toward High Performance All-Solid-State Lithium Batteries with High-Voltage Cathode Materials: Design Strategies for Solid Electrolytes, Cathode Interfaces, and Composite Electrodes. *Adv. Energy Mater.* **2021**, *11*, 2003154. [CrossRef]
4. Ali, S.M.; Arif, N.A.; Hashmi, M.M.; Khan, M.B.; Khan, Z.H. Recent Developments in Electrolyte Materials for Rechargeable Batteries. In *Nanomaterials for Innovative Energy Systems and Devices*; Khan, Z.H., Ed.; Materials Horizons: From Nature to Nanomaterials; Springer Nature Singapore: Singapore, 2022; pp. 369–415. ISBN 978-981-19055-2-0.
5. Su, Y.; Zhang, X.; Du, C.; Luo, Y.; Chen, J.; Yan, J.; Zhu, D.; Geng, L.; Liu, S.; Zhao, J.; et al. An All-Solid-State Battery Based on Sulfide and PEO Composite Electrolyte. *Small* **2022**, *18*, 2202069. [CrossRef] [PubMed]

6. Hou, Z.; Xia, S.; Niu, C.; Pang, Y.; Sun, H.; Li, Z.; Xu, Y.; Zheng, S. Tailoring the Interaction of Covalent Organic Framework with the Polyether Matrix toward High-performance Solid-state Lithium Metal Batteries. *Carbon Energy* **2022**, *4*, 506–516. [CrossRef]

7. Abdelmaoula, A.E.; Shu, J.; Cheng, Y.; Xu, L.; Zhang, G.; Xia, Y.; Tahir, M.; Wu, P.; Mai, L. Core–Shell MOF-in-MOF NanoporeBifunctional Host of Electrolyte for High-Performance Solid-State Lithium Batteries. *Small Methods* **2021**, *5*, 2100508. [CrossRef]

8. Oh, D.Y.; Nam, Y.J.; Park, K.H.; Jung, S.H.; Kim, K.T.; Ha, A.R.; Jung, Y.S. Slurry-Fabricable Li$^+$—Conductive Polymeric Binders for Practical All-Solid-State Lithium-Ion Batteries Enabled by Solvate Ionic Liquids. *Adv. Energy Mater.* **2019**, *9*, 1802927. [CrossRef]

9. Mauger, A.; Julien, C.M.; Paolella, A.; Armand, M.; Zaghib, K. Building Better Batteries in the Solid State: A Review. *Materials* **2019**, *12*, 3892. [CrossRef]

10. Zou, C.; Yang, L.; Luo, K.; Liu, L.; Tao, X.; Yi, L.; Liu, X.; Zhang, X.; Wang, X. In Situ Formed Protective Layer: Toward a More Stable Interface between the Lithium Metal Anode and Li$_6$PS$_5$Cl Solid Electrolyte. *ACS Appl. Energy Mater.* **2022**, *5*, 8428–8436. [CrossRef]

11. Chen, X.; Xie, J.; Zhao, X.; Zhu, T. Electrochemical Compatibility of Solid-State Electrolytes with Cathodes and Anodes for All-Solid-State Lithium Batteries: A Review. *Adv. Energy Sustain. Res.* **2021**, *2*, 2000101. [CrossRef]

12. Cong, L.; Li, Y.; Lu, W.; Jie, J.; Liu, Y.; Sun, L.; Xie, H. Unlocking the Poly(Vinylidene Fluoride-Co-Hexafluoropropylene)/ Li$_{10}$GeP$_2$S$_{12}$ Composite Solid-State Electrolytes for Dendrite-Free Li Metal Batteries Assisting with Perfluoropolyethers as Bifunctional Adjuvant. *J. Power Sources* **2020**, *446*, 227365. [CrossRef]

13. Xu, R.; Cheng, X.-B.; Yan, C.; Zhang, X.-Q.; Xiao, Y.; Zhao, C.-Z.; Huang, J.-Q.; Zhang, Q. Artificial Interphases for Highly Stable Lithium Metal Anode. *Matter* **2019**, *1*, 317–344. [CrossRef]

14. Zhao, C.-Z.; Zhao, B.-C.; Yan, C.; Zhang, X.-Q.; Huang, J.-Q.; Mo, Y.; Xu, X.; Li, H.; Zhang, Q. Liquid Phase Therapy to Solid Electrolyte–Electrode Interface in Solid-State Li Metal Batteries: A Review. *Energy Stor. Mater.* **2020**, *24*, 75–84. [CrossRef]

15. Tang, J.; Wang, L.; Tian, C.; Huang, T.; Zeng, L.; Yu, A. Comparative Performance of LiFePO$_4$ and LiNi$_{0.6}$Co$_{0.2}$Mn$_{0.2}$O$_2$ Cathode Materials for Lithium Batteries with Solid–Liquid Hybrid Electrolytes. *J. Power Sources* **2021**, *515*, 230639. [CrossRef]

16. Wang, C.; Sun, Q.; Liu, Y.; Zhao, Y.; Li, X.; Lin, X.; Banis, M.N.; Li, M.; Li, W.; Adair, K.R.; et al. Boosting the Performance of Lithium Batteries with Solid-Liquid Hybrid Electrolytes: Interfacial Properties and Effects of Liquid Electrolytes. *Nano Energy* **2018**, *48*, 35–43. [CrossRef]

17. Hatz, A.-K.; Calaminus, R.; Feijoo, J.; Treber, F.; Blahusch, J.; Lenz, T.; Reichel, M.; Karaghiosoff, K.; Vargas-Barbosa, N.M.; Lotsch, B.V. Chemical Stability and Ionic Conductivity of LGPS-Type Solid Electrolyte Tetra-Li$_7$SiPS$_8$ after Solvent Treatment. *ACS Appl. Energy Mater.* **2021**, *4*, 9932–9943. [CrossRef]

18. Yu, Q.; Han, D.; Lu, Q.; He, Y.-B.; Li, S.; Liu, Q.; Han, C.; Kang, F.; Li, B. Constructing Effective Interfaces for Li$_{1.5}$Al$_{0.5}$Ge$_{1.5}$ (PO$_4$)$_3$ Pellets To Achieve Room-Temperature Hybrid Solid-State Lithium Metal Batteries. *ACS Appl. Mater. Interfaces* **2019**, *11*, 9911–9918. [CrossRef]

19. Kim, M.-J.; Park, J.-W.; Kim, B.G.; Lee, Y.-J.; Ha, Y.-C.; Lee, S.-M.; Baeg, K.-J. Facile Fabrication of Solution-Processed Solid-Electrolytes for High-Energy-Density All-Solid-State-Batteries by Enhanced Interfacial Contact. *Sci. Rep.* **2020**, *10*, 11923. [CrossRef]

20. Zhang, Z.; Zhang, Q.; Shi, J.; Chu, Y.S.; Yu, X.; Xu, K.; Ge, M.; Yan, H.; Li, W.; Gu, L.; et al. A Self-Forming Composite Electrolyte for Solid-State Sodium Battery with Ultralong Cycle Life. *Adv. Energy Mater.* **2017**, *7*, 1601196. [CrossRef]

21. Oh, D.Y.; Ha, A.R.; Lee, J.E.; Jung, S.H.; Jeong, G.; Cho, W.; Kim, K.S.; Jung, Y.S. Wet-Chemical Tuning of Li$_{3-x}$PS$_4$ ($0 \leq x \leq 0.3$) Enabled by Dual Solvents for All-Solid-State Lithium-Ion Batteries. *ChemSusChem* **2020**, *13*, 146–151. [CrossRef]

22. Cao, Y.; Lou, S.; Sun, Z.; Tang, W.; Ma, Y.; Zuo, P.; Wang, J.; Du, C.; Gao, Y.; Yin, G. Solvate Ionic Liquid Boosting Favorable Interfaces Kinetics to Achieve the Excellent Performance of Li$_4$Ti$_5$O$_{12}$ Anodes in Li$_{10}$GeP$_2$S$_{12}$ Based Solid-State Batteries. *Chem. Eng. J.* **2020**, *382*, 123046. [CrossRef]

23. Fan, B.; Li, W.; Luo, Z.; Zhang, X.; Ma, H.; Fan, P.; Xue, B. Stabilizing Interface between Li$_2$S–P$_2$S$_5$ Glass-Ceramic Electrolyte and Ether Electrolyte by Tuning Solvation Reaction. *ACS Appl. Mater. Interfaces* **2022**, *14*, 933–942. [CrossRef] [PubMed]

24. Yan, S.; Abouali, S.; Yim, C.-H.; Zhou, J.; Wang, J.; Baranova, E.A.; Weck, A.; Thangadurai, V.; Merati, A.; Abu-Lebdeh, Y. Revealing the Role of Liquid Electrolytes in Cycling of Garnet-Based Solid-State Lithium-Metal Batteries. *J. Phys. Chem. C* **2022**, *126*, 14027–14035. [CrossRef]

25. Jeon, H.; Hoang, H.A.; Kim, D. Flexible PVA/BMIMOTf/LLZTO Composite Electrolyte with Liquid-Comparable Ionic Conductivity for Solid-State Lithium Metal Battery. *J. Energy Chem.* **2022**, *74*, 128–139. [CrossRef]

26. Zhang, W.; Nie, J.; Li, F.; Wang, Z.L.; Sun, C. A Durable and Safe Solid-State Lithium Battery with a Hybrid Electrolyte Membrane. *Nano Energy* **2018**, *45*, 413–419. [CrossRef]

27. Sen, S.; Trevisanello, E.; Niemöller, E.; Shi, B.-X.; Simon, F.J.; Richter, F.H. The Role of Polymers in Lithium Solid-State Batteries with Inorganic Solid Electrolytes. *J. Mater. Chem. A* **2021**, *9*, 18701–18732. [CrossRef]

28. Weiss, M.; Simon, F.J.; Busche, M.R.; Nakamura, T.; Schröder, D.; Richter, F.H.; Janek, J. From Liquid- to Solid-State Batteries: Ion Transfer Kinetics of Heteroionic Interfaces. *Electrochem. Energy Rev.* **2020**, *3*, 221–238. [CrossRef]

29. Banerjee, A.; Wang, X.; Fang, C.; Wu, E.A.; Meng, Y.S. Interfaces and Interphases in All-Solid-State Batteries with Inorganic Solid Electrolytes. *Chem. Rev.* **2020**, *120*, 6878–6933. [CrossRef]

30. Wang, P.; Qu, W.; Song, W.; Chen, H.; Chen, R.; Fang, D. Electro–Chemo–Mechanical Issues at the Interfaces in Solid-State Lithium Metal Batteries. *Adv. Funct. Mater.* **2019**, *29*, 1900950. [CrossRef]

31. Li, F.; Li, J.; Zhu, F.; Liu, T.; Xu, B.; Kim, T.-H.; Kramer, M.J.; Ma, C.; Zhou, L.; Nan, C.-W. Atomically Intimate Contact between Solid Electrolytes and Electrodes for Li Batteries. *Matter* **2019**, *1*, 1001–1016. [CrossRef]

32. Li, Y.; Arnold, W.; Jasinski, J.B.; Thapa, A.; Sumanasekera, G.; Sunkara, M.; Narayanan, B.; Druffel, T.; Wang, H. Interface Stability of LiCl-Rich Argyrodite Li$_6$PS$_5$Cl with Propylene Carbonate Boosts High-Performance Lithium Batteries. *Electrochim. Acta* **2020**, *363*, 137128. [CrossRef]

33. Chen, R.; Li, Q.; Yu, X.; Chen, L.; Li, H. Approaching Practically Accessible Solid-State Batteries: Stability Issues Related to Solid Electrolytes and Interfaces. *Chem. Rev.* **2020**, *120*, 6820–6877. [CrossRef] [PubMed]

34. Zhou, D.; Shanmukaraj, D.; Tkacheva, A.; Armand, M.; Wang, G. Polymer Electrolytes for Lithium-Based Batteries: Advances and Prospects. *Chem* **2019**, *5*, 2326–2352. [CrossRef]

35. Rollo-Walker, G.; Malic, N.; Wang, X.; Chiefari, J.; Forsyth, M. Development and Progression of Polymer Electrolytes for Batteries: Influence of Structure and Chemistry. *Polymers* **2021**, *13*, 4127. [CrossRef]

36. Boaretto, N.; Meabe, L.; Martinez-Ibañez, M.; Armand, M.; Zhang, H. Review—Polymer Electrolytes for Rechargeable Batteries: From Nanocomposite to Nanohybrid. *J. Electrochem. Soc.* **2020**, *167*, 070524. [CrossRef]

37. Meng, N.; Zhu, X.; Lian, F. Particles in Composite Polymer Electrolyte for Solid-State Lithium Batteries: A Review. *Particuology* **2022**, *60*, 14–36. [CrossRef]

38. Gao, Y.; Yan, Z.; Gray, J.L.; He, X.; Wang, D.; Chen, T.; Huang, Q.; Li, Y.C.; Wang, H.; Kim, S.H.; et al. Polymer–Inorganic Solid–Electrolyte Interphase for Stable Lithium Metal Batteries under Lean Electrolyte Conditions. *Nat. Mater.* **2019**, *18*, 384–389. [CrossRef]

39. Zhou, D.; Liu, R.; He, Y.-B.; Li, F.; Liu, M.; Li, B.; Yang, Q.-H.; Cai, Q.; Kang, F. SiO$_2$ Hollow Nanosphere-Based Composite Solid Electrolyte for Lithium Metal Batteries to Suppress Lithium Dendrite Growth and Enhance Cycle Life. *Adv. Energy Mater.* **2016**, *6*, 1502214. [CrossRef]

40. Baymuratova, G.R.; Slesarenko, A.A.; Yudina, A.V.; Yarmolenko, O.V. Conducting Properties of Nanocomposite Polymer Electrolytes Based on Polyethylene Glycol Diacrylate and SiO$_2$ Nanoparticles at the Interface with a Lithium Electrode. *Russ. Chem. Bull.* **2018**, *67*, 1648–1654. [CrossRef]

41. Su, S.; Ma, J.; Zhao, L.; Lin, K.; Li, Q.; Lv, S.; Kang, F.; He, Y. Progress and Perspective of the Cathode/Electrolyte Interface Construction in All-solid-state Lithium Batteries. *Carbon Energy* **2021**, *3*, 866–894. [CrossRef]

42. Yarmolenko, O.V.; Yudina, A.V.; Khatmullina, K.G. Nanocomposite Polymer Electrolytes for the Lithium Power Sources (a Review). *Russ. J. Electrochem.* **2018**, *54*, 325–343. [CrossRef]

43. Yao, P.; Yu, H.; Ding, Z.; Liu, Y.; Lu, J.; Lavorgna, M.; Wu, J.; Liu, X. Review on Polymer-Based Composite Electrolytes for Lithium Batteries. *Front. Chem.* **2019**, *7*, 522. [CrossRef] [PubMed]

44. Polymer and ceramic electrolytes for energy storage divices. In *Polymer Electrolytes for Energy Storage Devices*, 1st ed.; Raghavan, P.; Jabeen Fatima, M.J. (Eds.) CRC Press: Boca Raton, FL, USA; London, UK; New York, NY, USA, 2021; ISBN 978-1-00-314479-3.

45. Yudina, A.V.; Berezin, M.P.; Baymuratova, G.R.; Shuvalova, N.I.; Yarmolenko, O.V. Specific features of the synthesis and the physicochemical properties of nanocomposite polymer electrolytes based on poly(ethylene glycol) diacrylate with the introduction of SiO$_2$. *Russ. Chem. Bull.* **2017**, *66*, 1278–1283. [CrossRef]

46. Baymuratova, G.R.; Chernyak, A.V.; Slesarenko, A.A.; Tulibaeva, G.Z.; Volkov, V.I.; Yarmolenko, O.V. Specific Features of Ion Transport in New Nanocomposite Gel Electrolytes Based on Cross-Linked Polymers and Silica Nanoparicles. *Russ. J. Electrochem.* **2019**, *55*, 529–536. [CrossRef]

47. Yudina, A.V.; Baymuratova, G.R.; Tulibaeva, G.Z.; Litvinov, A.L.; Shestakov, A.F.; Yarmolenko, O.V. Conductivity Increase Effect in Nanocomposite Polymer Gel Electrolytes: Manifestation in the IR Spectra. *Russ. Chem. Bull.* **2020**, *69*, 1455–1462. [CrossRef]

48. Yarmolenko, O.V.; Khatmullina, K.G.; Baymuratova, G.R.; Tulibaeva, G.Z.; Bogdanova, L.M.; Shestakov, A.F. Causes of the Double Maximum Conductivity of Nanocomposite Polymer Electrolytes for Lithium Power Sources. *Mendeleev Commun.* **2018**, *28*, 41–43. [CrossRef]

49. Kumar, D.; Suleman, M.; Hashmi, S.A. Studies on Poly(Vinylidene Fluoride-Co-Hexafluoropropylene) Based Gel Electrolyte Nanocomposite for Sodium–Sulfur Batteries. *Solid State Ion.* **2011**, *202*, 45–53. [CrossRef]

50. Kumar, D.; Hashmi, S.A. Ion Transport and Ion–Filler-Polymer Interaction in Poly(Methyl Methacrylate)-Based, Sodium Ion Conducting, Gel Polymer Electrolytes Dispersed with Silica Nanoparticles. *J. Power Sources* **2010**, *195*, 5101–5108. [CrossRef]

51. Baymuratova, G.R.; Khatmullina, K.G.; Yudina, A.V.; Yarmolenko, O.V. Design of a Solid-State Lithium Battery Based on LiFePO$_4$ Cathode and Polymer Gel Electrolyte with Silicon Dioxide Nanoparticles. *Russ. J. Electrochem.* **2022**, *58*, 329–340. [CrossRef]

52. Rushing, J.C.; Leonik, F.M.; Kuroda, D.G. Effect of Solvation Shell Structure and Composition on Ion Pair Formation: The Case Study of LiTDI in Organic Carbonates. *J. Phys. Chem. C* **2019**, *123*, 25102–25112. [CrossRef]

53. Ponnuchamy, V.; Mossa, S.; Skarmoutsos, I. Solvent and Salt Effect on Lithium Ion Solvation and Contact Ion Pair Formation in Organic Carbonates: A Quantum Chemical Perspective. *J. Phys. Chem. C* **2018**, *122*, 25930–25939. [CrossRef]

54. Ravikumar, B.; Mynam, M.; Repaka, S.; Rai, B. Solvation Shell Dynamics Explains Charge Transport Characteristics of LIB Electrolytes. *J. Mol. Liq.* **2021**, *338*, 116613. [CrossRef]

55. Volkov, V.I.; Yarmolenko, O.V.; Chernyak, A.V.; Slesarenko, N.A.; Avilova, I.A.; Baymuratova, G.R.; Yudina, A.V. Polymer Electrolytes for Lithium-Ion Batteries Studied by NMR Techniques. *Membranes* **2022**, *12*, 416. [CrossRef]

56. Volkov, V.I.; Marinin, A.A. NMR Methods for Studying Ion and Molecular Transport in Polymer Electrolytes. *Russ. Chem. Rev.* **2013**, *82*, 248–272. [CrossRef]

57. Miranda-Quintana, R.A.; Smiatek, J. Beneficial Properties of Solvents and Ions for Lithium Ion and Post-Lithium Ion Batteries: Implications from Charge Transfer Models. *Electrochim. Acta* **2021**, *384*, 138418. [CrossRef]

58. Lee, H.; Hwang, S.; Kim, M.; Kwak, K.; Lee, J.; Han, Y.-K.; Lee, H. Why Does Dimethyl Carbonate Dissociate Li Salt Better Than Other Linear Carbonates? Critical Role of Polar Conformers. *J. Phys. Chem. Lett.* **2020**, *11*, 10382–10387. [CrossRef] [PubMed]

59. Zhang, S.S. Design Aspects of Electrolytes for Fast Charge of Li-ion Batteries. *InfoMat* **2021**, *3*, 125–130. [CrossRef]

60. Yao, N.; Chen, X.; Fu, Z.-H.; Zhang, Q. Applying Classical, *Ab Initio*, and Machine-Learning Molecular Dynamics Simulations to the Liquid Electrolyte for Rechargeable Batteries. *Chem. Rev.* **2022**, *122*, 10970–11021. [CrossRef]

61. Suh, K.-J.; Hong, Y.-S.; Skirda, V.D.; Volkov, V.I.; Lee, C.-Y.J.; Lee, C.-H. Water Self-Diffusion Behavior in Yeast Cells Studied by Pulsed Field Gradient NMR. *Biophys. Chem.* **2003**, *104*, 121–130. [CrossRef]

62. Hayamizu, K.; Aihara, Y. Ion and Solvent Diffusion and Ion Conduction of PC-DEC and PC-DME Binary Solvent Electrolytes of LiN(SO$_2$CF$_3$)$_2$. *Electrochim. Acta* **2004**, *49*, 3397–3402. [CrossRef]

63. Perdew, J.P.; Burke, K.; Ernzerhof, M. Generalized Gradient Approximation Made Simple. *Phys. Rev. Lett.* **1996**, *77*, 3865–3868. [CrossRef] [PubMed]

64. Stevens, W.J.; Basch, H.; Krauss, M.J. Valence basis set for transition metals (available Li-Rn) with corresponding ECPs. *J. Chem. Phys.* **1984**, *81*, 6026–6033. [CrossRef]

65. Laikov, D.N. A New Parametrizable Model of Molecular Electronic Structure. *J. Chem. Phys.* **2011**, *135*, 134120. [CrossRef]

66. Laikov, D.N. A New Class of Atomic Basis Functions for Accurate Electronic Structure Calculations of Molecules. *Chem. Phys. Lett.* **2005**, *416*, 116–120. [CrossRef]

67. Laikov, D.N. Fast Evaluation of Density Functional Exchange-Correlation Terms Using the Expansion of the Electron Density in Auxiliary Basis Sets. *Chem. Phys. Lett.* **1997**, *281*, 151–156. [CrossRef]

68. Hong, E.-S.; Okada, S.; Sonoda, T.; Gopukumar, S.; Yamaki, J. Thermal Stability of Electrolytes with Mixtures of LiPF$_6$ and LiBF$_4$ Used in Lithium-Ion Cells. *J. Electrochem. Soc.* **2004**, *151*, A1836. [CrossRef]

69. Yarmolenko, O.V.; Efimov, O.N.; Obolonkova, E.S.; Ponomarenko, A.T.; Kotova, A.V.; Matveeva, I.A.; Zapadinskii, B.I. Polymeric gel electrolyte based on oligo(urethane dimethacrylate) and poly(propylene glycol monomethacrylate): A study by scanning electron microscopy. *Polym. Sci. Ser. A* **2004**, *46*, 773.

70. Chang, Z.; Qiao, Y.; Deng, H.; Yang, H.; He, P.; Zhou, H. A Liquid Electrolyte with De-Solvated Lithium Ions for Lithium-Metal Battery. *Joule* **2020**, *4*, 1776–1789. [CrossRef]

71. Yilmazer, N.D.; Korth, M. Enhanced Semiempirical QM Methods for Biomolecular Interactions. *Comput. Struct. Biotechnol. J.* **2015**, *13*, 169–175. [CrossRef]